


Signatures of topotactic hydrogen in nickelate superconductors

Liang Si^{1,2,*} , Paul Worm² , Karsten Held^{2,*} 

¹ School of Physics, Northwest University, Xi'an 710069, China

² Institute for Solid State Physics, Vienna University of Technology, 1040 Vienna, Austria

* Correspondence: liang.si@ifp.tuwien.ac.at; held@ifp.tuwien.ac.at

Abstract: Superconductivity has entered the nickel age marked by enormous experimental and theoretical efforts. Notwithstanding, synthesizing nickelate superconductors remains extremely challenging, not least due to incomplete oxygen reduction and topotactic hydrogen. Here, we present density-functional theory calculations, identify a phonon mode as a possible indication for topotactic hydrogen and discuss the charge redistribution patterns around oxygen and hydrogen impurities.

Keywords: Superconductivity; nickelates; strongly correlated electron systems

1. Introduction

Computational materials calculations predicted superconductivity in nickelates [1] and heterostructures thereof [2–4] since decades, mainly based on apparent similarity to cuprate superconductors. Three years ago, superconductivity in nickelates was finally discovered in experiment by Li, Hwang and coworkers [5], breaking the grounds for a new age of superconductivity, the nickel age. It is marked by an enormous theoretical and experimental activity, including but not restricted to [5–31]. Superconductivity has been found by now, among others, in $\text{Nd}_{1-x}\text{Sr}_x\text{NiO}_2$ [5,6], $\text{Pr}_{1-x}\text{Sr}_x\text{NiO}_2$ [7], $\text{La}_{1-x}\text{Ca}_x\text{NiO}_2$ [8], $\text{La}_{1-x}\text{Sr}_x\text{NiO}_2$ [9], and most recently in the pentalayer nickelate $\text{Nd}_6\text{Ni}_5\text{O}_{12}$ [10]. Fig. 1 shows some of the hallmark experimental critical temperatures (T_c 's) for the nickelates in comparison with the preceding copper [32] and iron age [33] of unconventional superconductivity. Also shown are some other noteworthy superconductors, including the first superconductor, solid Hg, technologically relevant NbTi, and hydride superconductors [34]. The last are superconducting at room temperature [35], albeit only at a pressure of 267 GPa exerted in a diamond anvil cell. All of these compounds are marked in gray in Fig. 1 as they are conventional superconductors. That is, the pairing of electrons originates from the electron-phonon coupling, as described in the theory of Bardeen, Cooper, and Schrieffer (BCS) [36].

In contrast, cuprates, nickelates, and, to a lesser extent, iron pnictides are strongly correlated electron systems with a large Coulomb interaction between electrons because of their narrow transition metal orbitals. Their T_c is too high for BCS theory [37,38], and the origin of superconductivity in these strongly correlated systems is still hotly debated. One prospective mechanism are antiferromagnetic spin fluctuations [39–55] stemming from strong electronic correlations. Another mechanism is based on charge density wave fluctuations and received renewed interest with the discovery of charge density wave ordering in cuprates [56,57]. Dynamical vertex approximation [58–61] calculations for nickelates [27], that are unbiased with respect to charge and spin fluctuations, found that spin fluctuations dominate and successfully predicted the superconducting dome prior to experiment in $\text{Nd}_{1-x}\text{Sr}_x\text{NiO}_2$ [62–64].

Why did it take 20 years to synthesize superconducting nickelates that have been so seemingly predicted on a computer? To mimic the cuprate $\text{Cu } 3d^9$ configuration, as in NdNiO_2 , nickel has to be in the uncommon oxidation state Ni^{1+} which is rare and prone to oxidize further. Only through a complex two step procedure, Lee, Hwang and coworkers [65] were

arXiv:2204.10657v1 [cond-mat.supr-con] 22 Apr 2022



Citation: Liang, S.; Worm, P.; Held, K. Signatures of topotactic hydrogen in nickelates. *Preprints* 2021, 1, 0. <https://doi.org/>

Received:

Accepted:

Published:

Publisher's Note: XXX stays neutral with regard to jurisdictional claims in published maps and institutional affiliations.

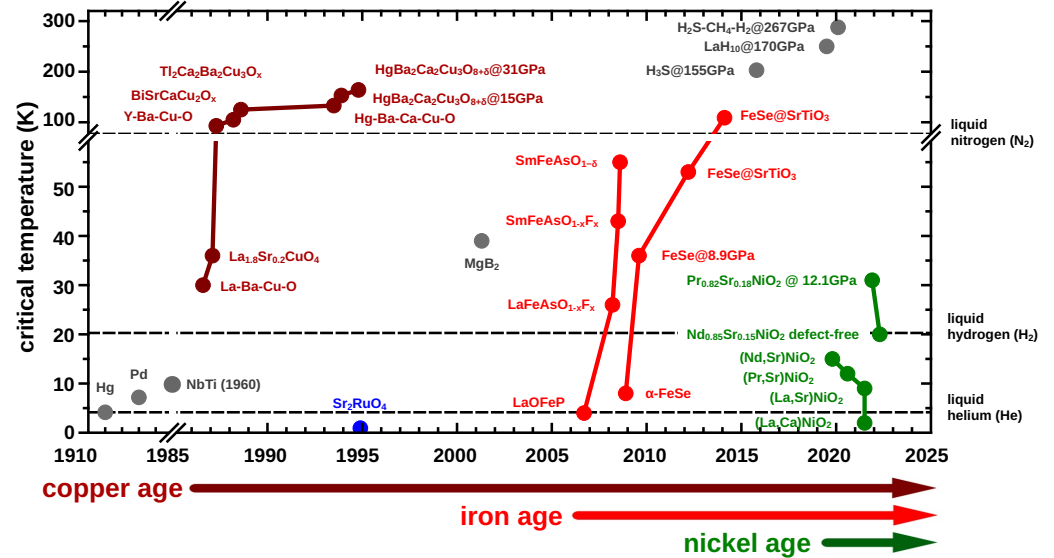


Figure 1. Superconducting T_c vs. year of discovery for selected superconductors. The discovery of cuprates, iron pnictides and nickelates led to enormous experimental and theoretical activities. Hence one also speaks of the copper, iron and nickel age of superconductivity.

able to synthesize superconducting nickelates. In a first step, modern pulsed laser deposition (PLD) was used to grow a $\text{Sr}_x\text{Nd}_{1-x}\text{NiO}_3$ film on a SrTiO_2 substrate. This nickelate is still in the 3D perovskite phase, see Fig. 2 (left), with one oxygen atom too much and will thus not show superconductivity. Hence, this additional oxygen between the layers needs to be removed in a second step. The reducing agent CaH_2 is used to this end, within a quite narrow temperature window [65]. If all goes well, one arrives at the superconducting $\text{Sr}_x\text{Nd}_{1-x}\text{NiO}_2$ film (top center). However, this process is prone to incomplete oxidation or to intercalate hydrogen topotactically, i.e., at the position of the removed oxygen, see Fig. 2 (bottom center). Both of those unwanted outcomes are detrimental for superconductivity.

In [21,67,68] it was shown by density functional theory (DFT) calculations that NdNiO_2H is indeed energetically favorable to $\text{NdNiO}_2 + 1/2 \text{H}$. For the doped system, on the other hand, $\text{Nd}_{0.8}\text{Sr}_{0.2}\text{NiO}_2$ without the hydrogen intercalated is energetically favorable. The additional H or likewise an incomplete oxidation to $\text{SrNdNiO}_{2.5}$ alters the physics completely. Additional H or $\text{O}_{0.5}$ will remove an electron from the Ni atoms, resulting in Ni^{2+} instead of Ni^{1+} . The formal electronic configuration is hence $3d^8$ instead of $3d^9$, or two holes instead of one hole in the Ni d -shell. Dynamical mean-field theory (DMFT) calculations [21] evidence that the basic atomic configuration is the one of Fig. 2 (lower right). That is, because of Hund's exchange the two holes in NdNiO_2H occupy two different orbitals, $3d_{x^2-y^2}$ and $3d_{3z^2-r^2}$, and form a spin-1. A consequence of this is that DMFT calculations predict NdNiO_2H to be a Mott insulator, whereas NdNiO_2 is a strongly correlated metal with a large mass enhancement of about five [21].

To the best of our knowledge, such a two-orbital, more 3D electronic structure is unfavorable for high- T_c superconductivity. The two-dimensionality of cuprate and nickelate superconductors helps to suppress long-range antiferromagnetic order, while at the same time retaining strong antiferromagnetic fluctuations that can act as a pairing glue for superconductivity. In experiment, we cannot expect ideal NdNiO_2 , NdNiO_2H or $\text{NdNiO}_{2.5}$ films, but most likely some H or additional O will remain in the NdNiO_2 film, after the CaH_2 reduction. Additional oxygen can be directly evidenced in standard x-ray diffraction analysis after the

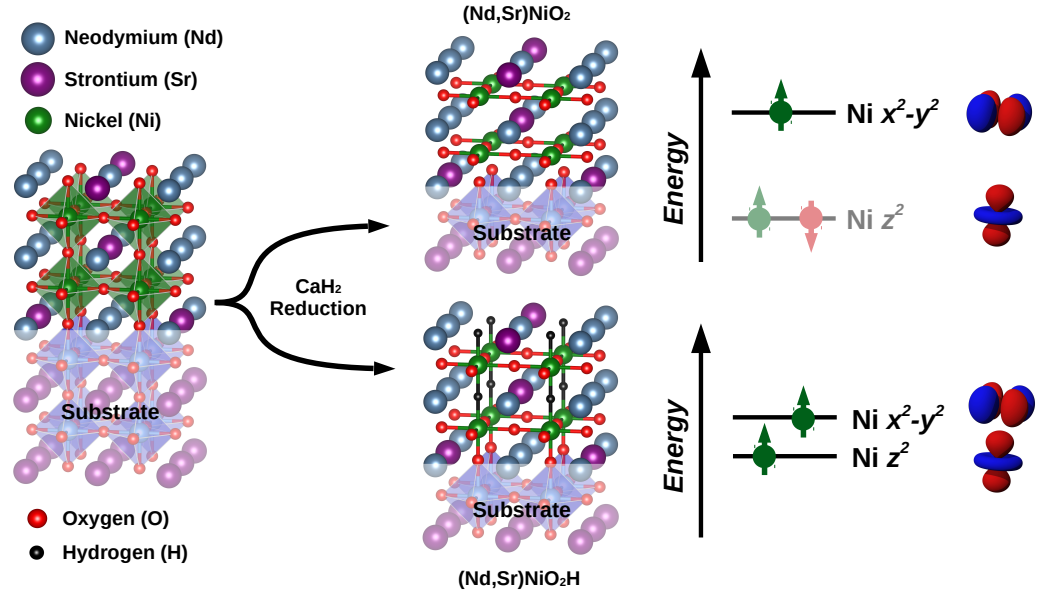


Figure 2. For synthesizing superconducting nickelates (1, left) a perovskite film of $\text{Nd}(\text{La})_{1-x}\text{Sr}_x\text{NiO}_3$ is grown on a SrTiO_3 substrate and (2, center) the O atoms between the planes are removed by reduction with CaH_2 . Besides the pursued nickelate $\text{Nd}(\text{La})_{1-x}\text{Sr}_x\text{NiO}_2$ (top center) also excess oxygen or topotactic H may remain in the film, yielding $\text{Nd}(\text{La})_{1-x}\text{Sr}_x\text{NiO}_2\text{H}$ (bottom center). The excess hydrogen results in two holes instead of one hole within the topmost two Ni $3d$ orbitals (right). Adapted from [66].

synthesis step. However, hydrogen, being very light, evades such an x-ray analysis. It has been evidenced in nickelates only by nuclear magnetic resonance (NMR) experiments [69] which, contrary to x-ray techniques, are very sensitive to hydrogen. Ref. [70] suggested hydrogen in LaNiO_2 to be confined at grain boundaries or secondary-phase precipitates. Given these difficulties, it is maybe not astonishing that it took almost one year before a second research group [6] was able to reproduce superconductivity in nickelates. Despite enormous experimental efforts, only a few groups succeeded hitherto.

In this paper, we present additional DFT results for topotactic hydrogen and incomplete oxygen reduction in nickelate superconductors: In Section 3 we provide technical information on the DFT calculations. In Section 3 we analyze the energy gain to topotactically intercalate hydrogen in LaNiO_2 and NdNiO_2 . In Section 4, we analyze the phonon spectrum and identify a high-energy mode originating from the Ni-H-Ni bond as a characteristic feature of intercalated hydrogen. In Section 5 we show the changes of the charge distribution caused by topotactic hydrogen. Finally, Section 6 provides a summary and outlook.

2. Method

Computational details on E_b . In both our previous theoretical study [21] and this article, the binding energy E_b of hydrogen atoms is computed as:

$$E_b = E[\text{ABO}_2] + \mu[\text{H}] - E[\text{ABO}_2\text{H}]. \quad (1)$$

Here, $E[\text{ABO}_2]$ and $E[\text{ABO}_2\text{H}]$ are the total energy of infinite-layer ABO_2 and hydride-oxides ABO_2H , while $\mu[\text{H}] = E[\text{H}_2]/2$ is the chemical potential of H. Note that H_2 is a typical byproduct for the reduction with CaH_2 and also emerges when CaH_2 is in contact with H_2O . Hence it can be expected to be present in the reaction. A positive (negative) E_b indicates

the topotactic H process is energetically favorable (unfavorable) to obtain ABO_2H instead of ABO_2 and $H_2/2$.

In the present paper, we go beyond [21] that reported E_b of various ABO_2 compounds by investigating E_b of $La_{1-x}Ca_xNiO_2$ systems for many different doping levels. Here, the increasing Ca-doping is achieved by using the virtual crystal approximation (VCA) [71,72] from $LaNiO_2$ ($x=0$) to $CaNiO_2$ ($x=1$). For each Ca concentration, structure relaxation and static total energy calculation is carried out for $La_{1-x}Ca_xNiO_2$ and $La_{1-x}Ca_xNiO_2H$ within the tetragonal space group $P4/mmm$. To this end, we use density-functional theory (DFT) [73,74] with the VASP code [75,76] and the generalized gradient approximations (GGA) of Perdew, Burke, and Ernzerhof (PBE) [77] and PBE revised for solids (PBEsol) [78]. For undoped $LaNiO_2$, the GGA-PBEsol relaxations predict its in-plane lattice constant as 3.890 Å which is close to that of the STO substrate: 3.905 Å. The computations for $La_{1-x}Ca_xNiO_2$ and $LaCoO_2$, $LaCuO_2$, $SrCoO_2$ and $SrNiO_2$ are performed without spin-polarization and a DFT+ U treatment [79], as the inclusion of Coulomb U and spin-polarization only slightly decreases the E_b by $\sim 5\%$ for $LaNiO_2$ [66]. For $NdNiO_2$, an inevitable computational issue are the localized Nd-4*f* orbitals. These *f*-orbitals are localized around the atomic core, leading to strong correlations. In non-spin-polarized DFT calculations this generates flat bands near the Fermi level E_F and leads to unsuccessful convergence. To avoid this, we employed DFT+ U [$U_f(Nd)=7$ eV and $U_d(Ni)=4.4$ eV] and initialize a G-type anti-ferromagnetic ordering for both Nd- and Ni-sublattice in a $\sqrt{2} \times \sqrt{2} \times 2$ supercell of $NdNiO_2$. For the $Nd_{0.75}Sr_{0.25}NiO_2$ case, 25% Sr-doping is achieved by replacing one out of the four Nd atoms by Sr in a $\sqrt{2} \times \sqrt{2} \times 2$ $NdNiO_2$ supercell.

Computational details on phonons. The phonon computations for $LaNiO_2$, $LaNiO_2H$, $LaNiO_2H_{0.125}$, $LaNiO_{2.125}$ are performed with the frozen phonon method using the PHONOPY [80] code interfaced with VASP. Computations with density functional perturbation theory (DFPT) method [81] are also carried out for double check. For $LaNiO_2$ and $LaNiO_2H$, the unit cells shown in Fig. 4(a,b) are enlarged to a $2 \times 2 \times 2$ supercell, while for $LaNiO_2H_{0.125}$ and $LaNiO_{2.125}$ the phonon are directly computed with the supercell of Fig. 4(c,d).

Computational details on electron density. The electron density distributions of $LaNiO_2$, $LaNiO_2H$, $LaNiO_2H_{0.125}$, and $LaNiO_{2.125}$ are computed using the WIEN2K code [82] while taking the VASP-relaxed crystal structure as input. The isosurfaces are plotted from 0.1 (yellow lines) to 2.0 (center of atoms) with spacing 0.1 in units of $e/\text{Å}^2$.

3. Energetic stability

Fig. 3 shows the results of the hydrogen binding energy E_b for the infinite layer nickelate superconductors $Nd_{1-x}Sr_xNiO_2$ [5,62,63] and $La_{1-x}Ca_xNiO_2$ [8]. To reveal the evolution of E_b when the B-site band filling deviates from their original configurations ($3d^9$ in $LaNiO_2$ when $x=0$ and $3d^8$ in $CaNiO_2$ when $x=1$), we also show the binding energy of $LaCoO_2$ ($3d^8$), $LaCuO_2$ ($3d^{10}$), $SrCoO_2$ ($3d^7$) and $SrNiO_2$ ($3d^8$).

Let us start with the case of $La_{1-x}Ca_xNiO_2$ [8]. Here, the unoccupied La-4*f* orbitals make the computation possible even without spin-polarization and Coulomb U for La-4*f*, whereas for $NdNiO_2$ this is not practicable due to Nd-4*f* flat bands near E_F . Positive (negative) E_b above (below) the horizontal line in Fig. 3 indicates topotactic H is energetically favorable (unfavorable). When $x=0$, i.e. for bulk $LaNiO_2$, the system tends to confine H atoms, resulting in oxide-hydride ABO_2H with $E_b = 157$ meV/H. As the concentration of Ca increases, E_b monotonously decreases, reaching -248 meV for the end member of the doping series, $CaNiO_2$. The turning point between favorable and unfavorable topotactic H inclusion is around 10% to 15% Ca-doping. Let us note that $E_b = 0$ roughly agrees with the onset of superconductivity, which for Ca-doped $LaNiO_2$ emerges for $x > 15\%$ Ca-doping [8].

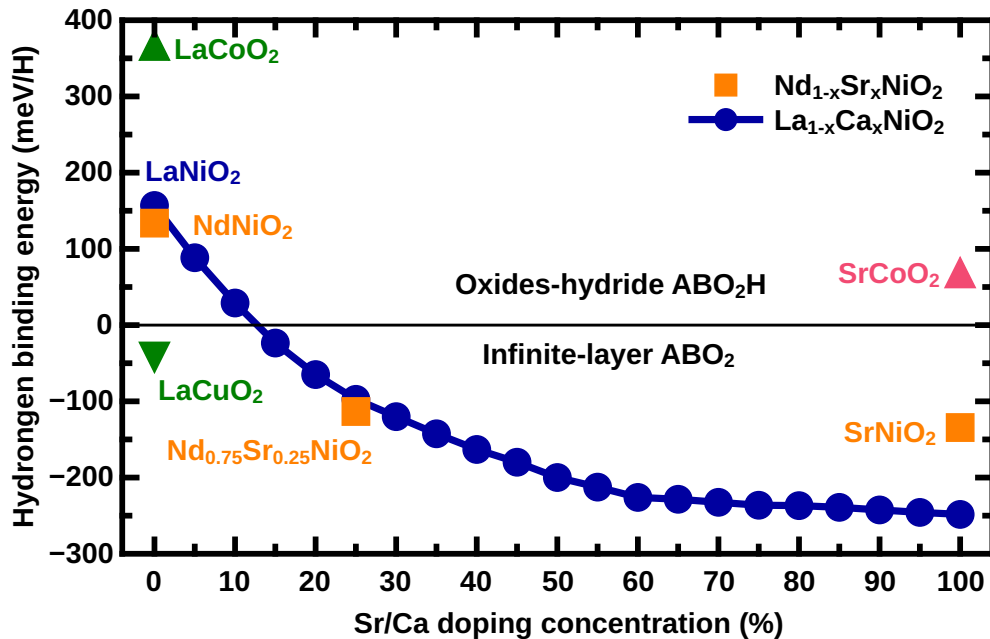


Figure 3. Hydrogen binding energy (E_b) per hydrogen in two nickelate superconductors, $(\text{La,Ca})\text{NiO}_2$ and $(\text{Nd,Sr})\text{NiO}_2$; LaCuO_2 , LaCoO_2 , and SrCoO_2 . Slightly above 10% (Sr,Ca) -doping infinite layer nickelates are energetically more stable. Note that the doping changes the filling of the B - $3d$ orbital. To study the relationship between E_b and the types of B -site elements, E_b of several other ABO_2 compounds is computed: LaCoO_2 , LaCuO_2 , SrCoO_2 and SrNiO_2 . Note that this changes the filling of B - $3d$ orbital within a large range: e.g. $3d^8$ for LaCoO_2 and $3d^9$ for LaNiO_2 .

To obtain E_b in NdNiO_2 a much higher computational effort is required: firstly, the $\text{Nd-}4f$ orbitals must be computed with either treating them as core-states or including spin-splitting. Secondly, for the spin-polarized DFT(+ U) calculations, an appropriate (anti-)ferromagnetic ordering has to be arranged for both Ni- and Nd-sublattices. In oxide-hydride ABO_2H compounds, the δ -type bond between Ni and H stabilizes a G -type anti-ferromagnetic order by driving the system from a quasi two-dimensional (2D) system to a three dimensional (3D) one [21]. Given the large computational costs of E_b for $\text{Nd}_{1-x}\text{Sr}_x\text{NiO}_2$ by using anti-ferromagnetic DFT+ U calculations for both $\text{Nd-}4f$ ($U \sim 7$ eV) and $\text{Ni-}3d$ ($U=4.4$ eV) orbitals, we merely show here the results of NdNiO_2 ($x=0$), $\text{Nd}_{0.75}\text{Sr}_{0.25}\text{NiO}_2$ ($x=0.25$) and SrNiO_2 ($x=1$), which are adopted from [21]. With 25% Sr-doping, the E_b of NdNiO_2 is reduced from 134 meV to -113 meV. Please note that E_b of $(\text{Nd,Sr})\text{NiO}_2$ is slightly smaller than in $(\text{La,Ca})\text{NiO}_2$, at least in the low doping range. This can be explained by shorter lattice constants in NdNiO_2 , in agreement with the finding [21] that compressive strain plays an important role at reducing E_b .

One can speculate that this suppression of topotactic hydrogen may also play a role when comparing the recently synthesized $(\text{Nd,Sr})\text{NiO}_2$ films on a $(\text{LaAlO}_3)_{0.3}(\text{Sr}_2\text{TaAlO}_6)_{0.7}$ (LSAT) substrate [64] with the previously employed SrTiO_3 (STO) substrate [62]. Lee *et al.* [64] reported cleaner films without defects and also a higher superconducting transition temperature $T_c \sim 20$ K for the LSAT film, as compared to $T_c = 15$ K and plenty of stacking fault defects for the STO substrate [62]. As for $(\text{La,Ca})\text{NiO}_2$, $E_b = 0$ falls in the region of the onset of the superconductivity for $(\text{Sr,Nd})\text{NiO}_2$, which is $x \sim 10\%$ Sr-doping in LSAT-strained

defect-free films [64] and $x \sim 12.5\%$ at SrTiO₃-substrate states [62]. Topotactic hydrogen might play a role in suppressing superconductivity in this doping region.

In Fig. 3, we further show additional infinite layer compounds LaCoO₂, LaCuO₂, SrCoO₂ and SrNiO₂ for comparison. Their E_b is predicted to be 367, -42, 69 and -134 meV, respectively. Combining the results of LaNiO₂ and CaNiO₂, we summarize several tendencies on how to predict E_b of ABO₂: (1) the strongest effect on E_b is changing the B-site element. However this seems unpractical for nickelate superconductors as the band filling is strictly restricted to be $3d^{9-x}$ ($x \sim 0.2$). For both trivalent (La, Nd) and bivalent (Sr, Ca) cations, E_b decreases when the B-site cation goes from early to late transition metal elements, e.g. from LaCoO₂ ($3d^8$) to LaNiO₂ ($3d^9$) to LaCuO₂ ($3d^{10}$). (2) Compressive strains induced by either substrate or external pressure can effectively reduce E_b and we believe that this might be used for growing defect-free films. (3) According to our theoretical calculations, E_b mainly depends on lattice parameters and band filling of the B-site $3d$ -orbitals, but much less on magnetic ordering and Coulomb interaction U .

4. Phonon dispersion

As revealed by previous DFT phonon spectra calculations [16], NdNiO₂ is dynamically stable. One of the very fundamental question would be whether topotactic H from over-reacted reduction and/or O from unaccomplished reductive reactions affect the lattice stability. To investigate this point, we perform DFT phonon calculations and analyze the lattice vibration induced by H/O intercalation, as shown in Fig. 4.

The phonon spectrum of LaNiO₂ [4(a)] is essentially the same as in Ref. [16], all the phonon frequencies are positive, indicating it is dynamically stable. In Fig. 4(b), the oxides-hydride LaNiO₂H is also predicted to be dynamically stable. Please note that the phonon dispersions between 0 and 20 THz are basically the same as those in LaNiO₂ [Fig. 4(a); note the different scale of the y -axis]. However, one can see new, additional vibration modes from the light H-atoms at frequencies of ~ 27 THz and ~ 43 THz. Among these vibrations, the double degenerate mode at lower frequency is generated by an in-plane (xy -plane) vibration of the topotactic H atom. There are two such in-plane vibrations of H atoms, either along the (100) or (110) direction (and symmetrically related directions), as indicated by the orange arrows in Fig. 4(b). The mode located at the higher frequency ~ 43 THz is, on the other hand, formed by an out-of-plane (z -direction) vibration and is singly degenerate.

We explain these phonon modes in detail by computing the bonding strength between H-1s–Ni- d_{z^2} and H-1s–La- d_{xy} orbitals. Our tight-binding calculations yields an electron hopping term of -1.604 eV between H-1s and Ni- d_{z^2} while it is -1.052 eV from La- d_{xy} to H-1s. That is, the larger H-1s–Ni- d_{z^2} overlap leads to a stronger δ -type bonding and, together with the shorter c -lattice constant, to a higher phonon energy. Additionally, the shorter c -lattice in LaNiO₂ should also play a role at forming a stronger H-1s–Ni- d_{z^2} bond.

In our previous analysis of the band character for LaNiO₂H [21], the H-1s bands were mainly located at two energy regions: a very flat band that is mostly from the H-1s itself at ~ -7 to -6 eV, and a hybridized band between H-1s and Ni- d_{z^2} at ~ -2 eV. Together with the higher phonon energy this indicates that the topotactic H atoms are mainly confined by a Ni sub-lattice via bonding and anti-bonding states formed by H-1s and Ni- d_{z^2} orbitals, instead of the La(Nd) sub-lattice.

The complete (full) topotactic inclusion of H, where all vacancies induced by removing oxygen are filled by H, is an ideal limiting case. Under varying experimental conditions, such as chemical reagent, substrate, temperature, and strain, the H-topotactic inclusion may be incomplete, and thus ABO₂H _{δ} ($\delta < 1$) be energetically favored. Hence, we also compute the phonon spectrum at a rather low H-topotactic density: LaNiO₂H_{0.125}, achieved by including a single H into $2 \times 2 \times 2$ LaNiO₂ supercells as shown in Fig. 4(c). Also such a local H defect,

as revealed by the positive frequency at all q -vectors in the lower panel of Fig. 4(c), does not destroy the dynamical stability of the LaNiO_2 crystal. In fact, the only remarkable qualitative difference between the complete and 12.5% topotactic H case is the number of phonon bands at 0 THz to 20 THz. This is just a consequence of the larger $2 \times 2 \times 2$ LaNiO_2 supercell, with eight times more phonons. Some quantitative differences can be observed with respect to the energy of the phonon mode: The out-of-plane vibration energy is enhanced from ~ 43 THz in LaNiO_2H [Fig. 4(b)] to ~ 47 THz in $\text{LaNiO}_2\text{H}_{0.125}$ [Fig. 4(b)], and the in-plane vibration mode frequency is reduced from ~ 27 THz in LaNiO_2H [Fig. 4(b)] to ~ 21 THz $\text{LaNiO}_2\text{H}_{0.125}$ [Fig. 4(c)]. This is because the H-intercalation shrinks the local c -lattice, i.e., the distance between two Ni atoms separated by topotactic H, from 3.383 \AA in $[\text{LaNiO}_2\text{H}]$: Fig. 4(b)] to 3.327 \AA [$\text{LaNiO}_2\text{H}_{0.125}$: Fig. 4(c)]. The bond length between H and La is, on the other hand, slightly increased from 2.767 \AA in $[\text{LaNiO}_2\text{H}]$: Fig. 4(b)] to 2.277 \AA [$\text{LaNiO}_2\text{H}_{0.125}$: Fig. 4(c)]. This lattice compression (enlargement) explains the enhancement (reduction) for the out-of-plane (in-plane) phonon frequencies (energies).

These results pave a new way to detect the formation of topotactic H in infinite nickelate superconductors: by measuring the phonon modes. The existence of localized phonon modes with little dispersion at ~ 25 THz and ~ 45 THz indicates the presence of topotactic hydrogen, which otherwise would be extremely hard to detect. These frequencies correspond to energies of 103 meV and 186 meV, respectively, beyond the range < 80 meV measured for $\text{La}_{1-x}\text{Sr}_x\text{NiO}_2$ in [83].

Lastly, we further study the case representing an incompleting reduction process: $\text{LaNiO}_{2.125}$, achieved by intercalating a single O into a $2 \times 2 \times 2$ LaNiO_2 supercell [$\text{LaNiO}_{2.125}$: Fig. 4(d)]. As the same consequence of employing a supercell in phonon computation, the number of phonon bands is multiplied by a factor of 8 in the frequency region between 0 THz to 20 THz. One obvious difference between undoped LaNiO_2 [Fig. 4(a)] and $\text{LaNiO}_{2.125}$ [Fig. 4(d)] is, that the additional O leads to an unstable phonon mode near $q=X(\pi,0,0)$ [blue region in Fig. 4(d)]. This phonon mode is formed by an effective vibration of the additional O along the xy plane in the (001) or (110) direction (and symmetrically related directions depending on the exact q -vector) of locally cubic coordinate. Such a mode is related to the structural transition from cubic $Pm\bar{3}m$ to a $R\bar{3}c$ rhombohedral phase as in bulk LaNiO_3 , with the Ni-O-Ni bond along the z -direction deviating from 180° . Our simulations for other concentrations of additional O atoms (not shown) also indicate that incomplete oxygen reduction reactions generally result in local instabilities of $\text{LaNiO}_{2+\delta}$ with $\delta > 0$.

5. Charge distribution

In this Section, we perform electron density calculations for LaNiO_2 , LaNiO_2H , $\text{LaNiO}_2\text{H}_{0.125}$ and $\text{LaNiO}_{2.125}$ compounds to investigate the bond types resulting from intercalated H and O atoms. Fig. 5 (a) and (b) show the electron density of LaNiO_2 at the NiO-plane and La-plane (light green planes of the top panels). In Fig. 5(a), a strong Ni-O bond is observed while the low electron density between each Ni-O layers reveals a very weak inter-layer coupling, indicating the strong quasi-2D nature of the infinite layer nickelates. In Fig. 5(b), no bonds are formed between the La (Nd) atoms. The A-site rare-earth elements merely play the role of electron donors.

Fig. 5 (c) and (d) present the electron density of LaNiO_2H along the same planes. In the NiOH-plane of Fig. 5(c), the comparison to Fig. 5(a) shows that intercalated H boosts a 3D picture with an additional δ -type bond formed by Ni- d_{z^2} and H-1s orbitals (black circle). Along the LaH-plane [Fig. 5(d)], δ -type bonds are formed by the orbital overlap between La- d_{xy} and H-1s orbitals. For LaNiO_2 with partial topotactic H [$\text{LaNiO}_2\text{H}_{0.125}$ in Fig. 5(e,f)], the additional H atoms play similar roles at the Ni-H and the La-H bonds as in LaNiO_2H . The Ni and La atoms without H in-between are similar as in Fig. 5(a-b) and those with H are akin

to Fig. 5(c-d). This indicates that the effects induced by topotactic H are indeed very local, i.e., they only affect the the nearest Ni and La atoms.

In Fig. 5 (g) and (h), for $\text{LaNiO}_{2.125}$, the additional O increases the local c -lattice (Ni-Ni bond length via the additional O) from the LaNiO_2 value of 3.338 \AA to 4.018 \AA which is even larger than the DFT-relaxed value of LaNiO_3 : 3.80 \AA . This lattice expansion can be clearly seen in Fig. 5(g). The large electron density between Ni and O along the z -direction indicates the strength of this Ni-O bond in the z -direction is comparable with the ones along x/y directions. From Fig. 5(h), we conclude that similar La-O bonds are formed after intercalating additional O atoms, the La-La distance is shrunken by the additional O atom from 3.889 \AA (LaNiO_2) to 3.746 \AA between the La atoms pointing to the additional O. However, from the electron density plot, the La-O bond strength seems not stronger than the La-H bonding in Fig. 5(c,e). This can be explained by the fact that both $O-p_x$ and $-p_y$ orbitals do not point to orbital lobes of $\text{La}-d_{xy}$, leading to a comparable bond strength as the La-H bond in LaNiO_2H_x .

6. Conclusion and outlook

Our theoretical study demonstrates that the parent compounds of infinite-layer nickelate superconductors, LaNiO_2 and NdNiO_2 , are energetically unstable with respect to topotactic H in the reductive process from perovskite $\text{La}(\text{Nd})\text{NiO}_3$ to $\text{La}(\text{Nd})\text{NiO}_2$. The presence of H, which reshapes the systems from ABO_2 to the hydride-oxide ABO_2H , triggers a transition from a quasi-2D strongly correlated single-band ($d_{x^2-y^2}$) metal, to a 2-band ($d_{x^2-y^2}+d_{z^2}$) anti-ferromagnetic 3D Mott insulator. Our predictions [21] have been reproduced by other groups using DFT+ U calculations for other similar ABO_2 systems [67,68]. The recent experimental observation [84] of Ni^{2+} ($3d^8$) in nickelates indicates the existence of topotactic H, as do NMR experiments [69]. The presence of H and its consequence of a 3D Mott-insulator is unfavorable for the emergence of superconductivity in nickelates. However, it is difficult to detect topotactic H in experiment. Three factors contribute to this difficulty: (1) the small radius of H makes it hard to be detected by commonly employed experimental techniques such as x-ray diffraction and scanning transmission electron microscopy (STEM). (2) As revealed by our phonon calculations, the dynamical stability of $\text{La}(\text{Nd})\text{NiO}_2$ does not rely on the concentration of intercalated H atoms. Hence the same infinite-layer structures should be detected by STEM even in the presence of H. (3) As revealed by electron density distributions, the topotactic H does not break the local crystal structure either (e.g. bond length and angle); the H atoms merely affect the most nearby Ni atoms via a $\text{Ni}-d_{z^2}-\text{H}-1s$ δ -bond. This is different if we have additional O atoms instead of H: O atoms do not only induce a dynamical instability but also obviously change the local crystal by enlarging the Ni-Ni bond length and angle visibly. Oxygen impurities also lead to unstable phonon modes in LaNiO_{2+x} and thus a major lattice reconstruction.

The ways to avoid topotactic H revealed by our calculations are: in-plane compressive strains and bivalent cation doping with Sr or Ca. This draws our attention to the recently synthesized $(\text{Nd,Sr})\text{NiO}_2$ films [64], which has been grown on a $(\text{LaAlO}_3)_{0.3}(\text{Sr}_2\text{TaAlO}_6)_{0.7}$ (LSAT) instead of a SrTiO_3 (STO) substrate, inducing an additional 0.9% compressive strain. These new films were shown to be defect-free and with a considerably larger superconducting dome from 10% to 30% Sr-doping and a higher maximal $T_c \sim 20 \text{ K}$ [64], compared to 12.5%-25% Sr-doping and $T_c \sim 15 \text{ K}$ for nickelate films grown on STO which show many stacking faults [5,62,63]. The compressive strain induced by replacing the STO substrate ($a=3.905 \text{ \AA}$) by LSAT ($a=3.868 \text{ \AA}$) may tune the positive E_b to negative, thus contributing to suppressing defects and recovering a single $d_{x^2-y^2}$ -band picture.

Besides avoiding topotactic H, compressive strain is also predicted as an effectively way to enhance T_c . Previous dynamical vertex approximation calculations [27,66] reveal the key to enhance T_c in nickelates is to enhance the bandwidth W and to reduce the ratio

of Coulomb interaction U to W . Based on this prediction, we have proposed [27,66] three experimental ways to enhance T_c in nickelates: (1) in-plane compressive strain, which can indeed be achieved by using other substrates having a smaller lattice than STO, such as LSAT (3.868 Å), LaAlO₃ (3.80 Å) or SrLaAlO₄ (3.75 Å). The smaller in-plane lattice shrinks the distance between Ni atoms thus increases their orbital overlap, leading to a larger W and a smaller U/W . Recent experimental reports have confirmed the validity of this approach by growing (Nd,Sr)NiO₂ on LSAT [64] and Pr_{0.8}Sr_{0.2}NiO₂ on LSAT [85]. (2) Applying external pressure on the films plays the same role as in-plane strain for the, essentially 2D, nickelates. This has been experimentally realized in [86]: under 12.1 GPa pressure T_c can be enhanced monotonously to 31 K without yet showing a saturation. (3) Replacing 3d Ni by 4d Pd. In infinite-layer palladates such as NdPdO₂ or LaPdO₂ and similar compounds with 2D PdO₂ layers and separating layers between them, the more extended 4d orbitals of Pd are expected to reduce U/W from $U/W \sim 7$ for nickelates to $U/W \sim 6$ for palladates. Further experimental and theoretical research on the electronic and magnetic structure and the superconductive properties of palladates are thus worth to perform.

Acknowledgements We thank M. Kitatani, J. Tomczak, and Z. Zhong for valuable discussions and the Austrian Science Funds (FWF) for funding through project P 32044.

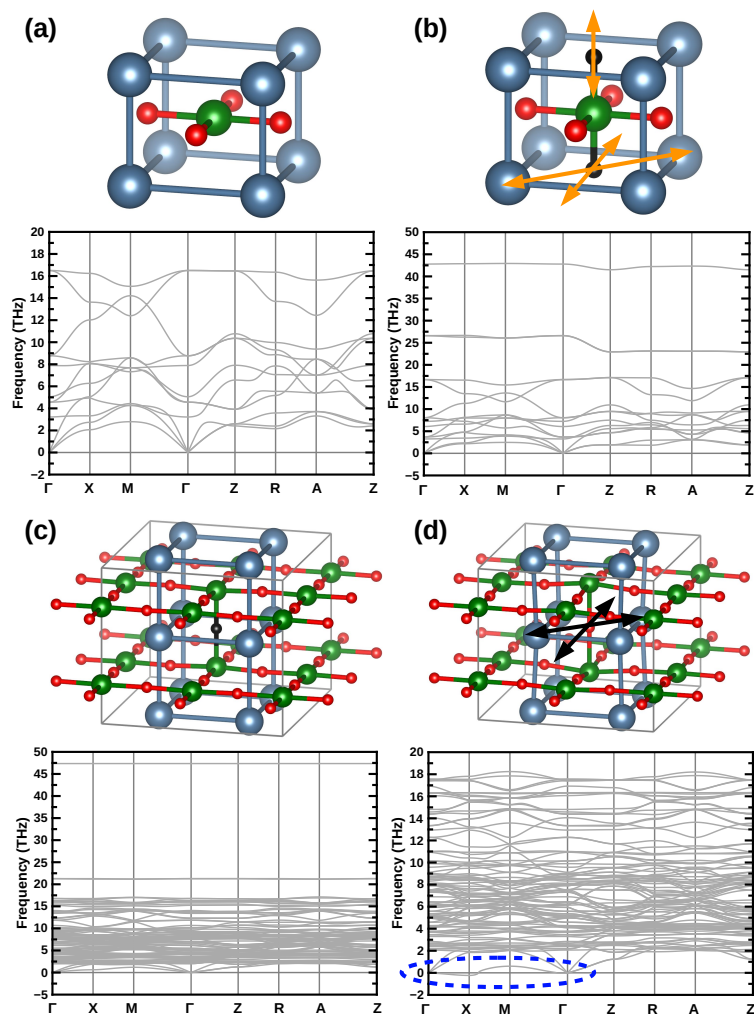


Figure 4. Phonon spectra of (a) LaNiO_2 , (b) LaNiO_2H and in a $2 \times 2 \times 2$ LaNiO_2 supercell doped with a single (c) H and (d) O atom [i.e. $\text{LaNiO}_2\text{H}_{0.125}$ in (c) and $\text{LaNiO}_{2.125}$ in (d)]. The orange and black arrows in (b) and (d) represent vibrations of H and O atoms. The blue dashed oval in (d) labels the unstable phonon modes induced by intercalating additional O atoms in LaNiO_2 .

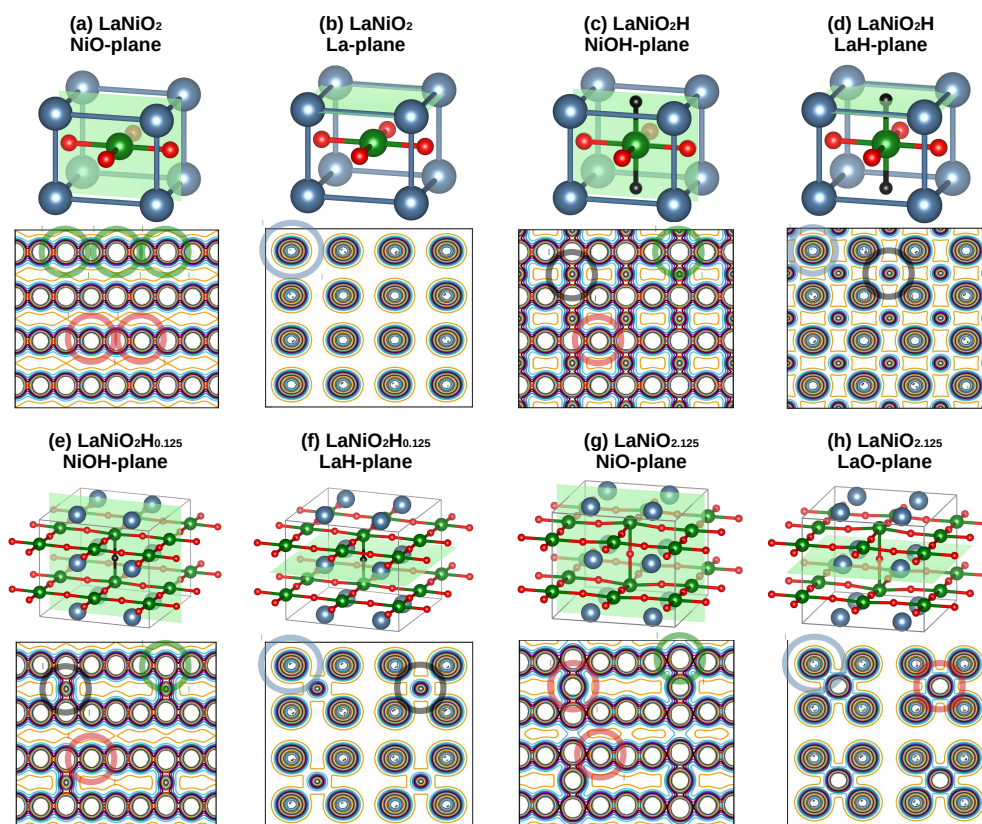


Figure 5. DFT calculated valence charge density of (a,b) LaNiO_2 , (c,d) LaNiO_2H , and a LaNiO_2 supercell doped with a single (e,f) H and (g,h) O atom. For each compound, the charge density of (020) and (001) planes are shown in panels (a,c,e,g) and (b,d,f,h), respectively. The La, Ni, O and H atoms are labeled by blue, green, red and black circles, respectively.

References

1. Anisimov, V.I.; Bukhvalov, D.; Rice, T.M. Electronic structure of possible nickelate analogs to the cuprates. *Phys. Rev. B* **1999**, *59*, 7901–7906. doi:10.1103/PhysRevB.59.7901.
2. Chaloupka, J.; Khaliullin, G. Orbital Order and Possible Superconductivity in LaNiO₃/LaMO₃ Superlattices. *Physical Review Letters* **2008**, *100*, 016404. doi:10.1103/PhysRevLett.100.016404.
3. Hansmann, P.; Yang, X.; Toschi, A.; Khaliullin, G.; Andersen, O.K.; Held, K. Turning a Nickelate Fermi Surface into a Cupratelike One through Heterostructuring. *Phys. Rev. Lett.* **2009**, *103*, 016401. doi:10.1103/PhysRevLett.103.016401.
4. Hansmann, P.; Toschi, A.; Yang, X.; Andersen, O.; Held, K. Electronic structure of nickelates: From two-dimensional heterostructures to three-dimensional bulk materials. *Phys. Rev. B* **2010**, *82*, 235123. doi:10.1103/PhysRevB.82.235123.
5. Li, D.; Lee, K.; Wang, B.Y.; Osada, M.; Crossley, S.; Lee, H.R.; Cui, Y.; Hikita, Y.; Hwang, H.Y. Superconductivity in an infinite-layer nickelate. *Nature* **2019**, *572*, 624–627. doi:10.1038/s41586-019-1496-5.
6. Zeng, S.; Tang, C.S.; Yin, X.; Li, C.; Li, M.; Huang, Z.; Hu, J.; Liu, W.; Omar, G.J.; Jani, H.; Lim, Z.S.; Han, K.; Wan, D.; Yang, P.; Pennycook, S.J.; Wee, A.T.S.; Ariando, A. Phase Diagram and Superconducting Dome of Infinite-Layer Nd_{1-x}Sr_xNiO₂ Thin Films, arXiv:2004.11281. *Phys. Rev. Lett.* **2020**, *125*, 147003. doi:10.1103/PhysRevLett.125.147003.
7. Osada, M.; Wang, B.Y.; Lee, K.; Li, D.; Hwang, H.Y. Phase diagram of infinite layer praseodymium nickelate Pr_{1-x}Sr_xNiO₂ thin films. *Phys. Rev. Materials* **2020**, *4*, 121801. doi:10.1103/PhysRevMaterials.4.121801.
8. Zeng, S.; Li, C.; Chow, L.E.; Cao, Y.; Zhang, Z.; Tang, C.S.; Yin, X.; Lim, Z.S.; Hu, J.; Yang, P.; others. Superconductivity in infinite-layer nickelate La_{1-x}CaxNiO₂ thin films. *Science advances* **2022**, *8*, eabl9927.
9. Osada, M.; Wang, B.Y.; Goodge, B.H.; Harvey, S.P.; Lee, K.; Li, D.; Kourkoutis, L.F.; Hwang, H.Y. Nickelate Superconductivity without Rare-Earth Magnetism: (La, Sr)NiO₂. *Advanced Materials* **2021**, *n/a*, 2104083. doi:10.1002/adma.202104083.
10. Pan, G.A.; Segedin, D.F.; LaBollita, H.; Song, Q.; Nica, E.M.; Goodge, B.H.; Pierce, A.T.; Doyle, S.; Novakov, S.; Carrizales, D.C.; N'Diaye, A.T.; Shafer, P.; Paik, H.; Heron, J.T.; Mason, J.A.; Yacoby, A.; Kourkoutis, L.F.; Erten, O.; Brooks, C.M.; Botana, A.S.; Mundy, J.A. Superconductivity in a quintuple-layer square-planar nickelate. *Nature Materials* **2021**. doi:10.1038/s41563-021-01142-9.
11. Botana, A.S.; Norman, M.R. Similarities and Differences between LaNiO₂ and CaCuO₂ and Implications for Superconductivity. *Phys. Rev. X* **2020**, *10*, 011024. doi:10.1103/PhysRevX.10.011024.
12. Sakakibara, H.; Usui, H.; Suzuki, K.; Kotani, T.; Aoki, H.; Kuroki, K. Model Construction and a Possibility of Cupratelike Pairing in a New *d*⁹ Nickelate Superconductor (Nd, Sr)NiO₂. *Phys. Rev. Lett.* **2020**, *125*, 077003. doi:10.1103/PhysRevLett.125.077003.
13. Hirayama, M.; Tadano, T.; Nomura, Y.; Arita, R. Materials design of dynamically stable *d*⁹ layered nickelates. *Phys. Rev. B* **2020**, *101*, 075107. doi:10.1103/PhysRevB.101.075107.
14. Hu, L.H.; Wu, C. Two-band model for magnetism and superconductivity in nickelates. *Phys. Rev. Research* **2019**, *1*, 032046. doi:10.1103/PhysRevResearch.1.032046.
15. Wu, X.; Di Sante, D.; Schwemmer, T.; Hanke, W.; Hwang, H.Y.; Raghu, S.; Thomale, R. Robust *d*_{x²-y²-wave superconductivity of infinite-layer nickelates. *Phys. Rev. B* **2020**, *101*, 060504. doi:10.1103/PhysRevB.101.060504.}
16. Nomura, Y.; Hirayama, M.; Tadano, T.; Yoshimoto, Y.; Nakamura, K.; Arita, R. Formation of a two-dimensional single-component correlated electron system and band engineering in the nickelate superconductor NdNiO₂. *Phys. Rev. B* **2019**, *100*, 205138. doi:10.1103/PhysRevB.100.205138.
17. Zhang, G.M.; Yang, Y.F.; Zhang, F.C. Self-doped Mott insulator for parent compounds of nickelate superconductors. *Phys. Rev. B* **2020**, *101*, 020501. doi:10.1103/PhysRevB.101.020501.
18. Jiang, M.; Berciu, M.; Sawatzky, G.A. Critical Nature of the Ni Spin State in Doped NdNiO₂. *Phys. Rev. Lett.* **2020**, *124*, 207004. doi:10.1103/PhysRevLett.124.207004.
19. Werner, P.; Hoshino, S. Nickelate superconductors: Multiorbital nature and spin freezing. *Phys. Rev. B* **2020**, *101*, 041104. doi:10.1103/PhysRevB.101.041104.
20. Lechermann, F. Late transition metal oxides with infinite-layer structure: Nickelates versus cuprates. *Phys. Rev. B* **2020**, *101*, 081110. doi:10.1103/PhysRevB.101.081110.
21. Si, L.; Xiao, W.; Kaufmann, J.; Tomczak, J.M.; Lu, Y.; Zhong, Z.; Held, K. Topotactic Hydrogen in Nickelate Superconductors and Akin Infinite-Layer Oxides ABO₂. *Phys. Rev. Lett.* **2020**, *124*, 166402. doi:10.1103/PhysRevLett.124.166402.
22. Lechermann, F. Multiorbital Processes Rule the Nd_{1-x}Sr_xNiO₂ Normal State. *Phys. Rev. X* **2020**, *10*, 041002. doi:10.1103/PhysRevX.10.041002.
23. Petocchi, F.; Christiansson, V.; Nilsson, F.; Aryasetiawan, F.; Werner, P. Normal State of Nd_{1-x}Sr_xNiO₂ from Self-Consistent GW + EDMFT. *Phys. Rev. X* **2020**, *10*, 041047. doi:10.1103/PhysRevX.10.041047.
24. Adhikary, P.; Bandyopadhyay, S.; Das, T.; Dasgupta, I.; Saha-Dasgupta, T. Orbital-selective superconductivity in a two-band model of infinite-layer nickelates. *Phys. Rev. B* **2020**, *102*, 100501. doi:10.1103/PhysRevB.102.100501.
25. Bandyopadhyay, S.; Adhikary, P.; Das, T.; Dasgupta, I.; Saha-Dasgupta, T. Superconductivity in infinite-layer nickelates: Role of *f* orbitals. *Phys. Rev. B* **2020**, *102*, 220502. doi:10.1103/PhysRevB.102.220502.
26. Karp, J.; Botana, A.S.; Norman, M.R.; Park, H.; Zingl, M.; Millis, A. Many-Body Electronic Structure of NdNiO₂ and CaCuO₂. *Phys. Rev. X* **2020**, *10*, 021061. doi:10.1103/PhysRevX.10.021061.

27. Kitatani, M.; Si, L.; Janson, O.; Arita, R.; Zhong, Z.; Held, K. Nickelate superconductors – a renaissance of the one-band Hubbard model, arXiv:2002.12230. *npj Quantum Materials* **2020**, *5*, 59. doi:10.1038/s41535-020-00260-y.
28. Worm, P.; Si, L.; Kitatani, M.; Arita, R.; Tomczak, J.M.; Held, K. Correlations turn electronic structure of finite-layer nickelates upside down. *arXiv:2111.12697* **2021**.
29. Geisler, B.; Pentcheva, R. Correlated interface electron gas in infinite-layer nickelate versus cuprate films on SrTiO₃(001). *Phys. Rev. Research* **2021**, *3*, 013261. doi:10.1103/PhysRevResearch.3.013261.
30. Klett, M.; Hansmann, P.; Schäfer, T. Magnetic Properties and Pseudogap Formation in Infinite-Layer Nickelates: Insights From the Single-Band Hubbard Model. *Frontiers in Physics* **2022**, *10*. doi:10.3389/fphy.2022.834682.
31. LaBollita, H.; Botana, A.S. Correlated electronic structure of a quintuple-layer nickelate. *Phys. Rev. B* **2022**, *105*, 085118. doi:10.1103/PhysRevB.105.085118.
32. Bednorz, J.G.; Müller, K.A. Possible high T_C superconductivity in the Ba–La–Cu–O system. *Zeitschrift für Physik B Condensed Matter* **1986**, *64*, 189–193.
33. Kamihara, Y.; Watanabe, T.; Hirano, M.; Hosono, H. Iron-Based Layered Superconductor La[O_{1-x}F_x]FeAs ($x = 0.05 - 0.12$) with T_C = 26K. *J. Am. Chem. Soc.* **2008**, *130*, 3296.
34. Drozdov, A.P.; Eremets, M.I.; Troyan, I.A.; Ksenofontov, V.; Shylin, S.I. Conventional superconductivity at 203 kelvin at high pressures in the sulfur hydride system. *Nature* **2015**, *512*, 73. doi:10.1038/s41563-021-01142-9.
35. Snider, E.; Dasenbrock-Gammon, N.; McBride, R.; Debessai, M.; Vindana, H.; Vencatasamy, K.; Salamat, K.V.L.A.; Dias, R.P. Room-temperature superconductivity in a carbonaceous sulfur hydride. *Nature* **2020**, *586*, 373. doi:10.1038/s41586-020-2801-z.
36. Bardeen, J.; Cooper, L.N.; Schrieffer, J.R. Microscopic Theory of Superconductivity. *Phys. Rev.* **1957**, *106*, 162–164. doi:10.1103/PhysRev.106.162.
37. Savrasov, S.Y.; Andersen, O.K. Linear-Response Calculation of the Electron-Phonon Coupling in Doped CaCuO₂. *Phys. Rev. Lett.* **1996**, *77*, 4430–4433. doi:10.1103/PhysRevLett.77.4430.
38. Boeri, L.; Dolgov, O.V.; Golubov, A.A. Is LaFeAsO_{1-x}F_x an Electron-Phonon Superconductor? *Phys. Rev. Lett.* **2008**, *101*, 026403. doi:10.1103/PhysRevLett.101.026403.
39. Scalapino, D.J. A common thread: The pairing interaction for unconventional superconductors. *Rev. Mod. Phys.* **2012**, *84*, 1383–1417. doi:10.1103/RevModPhys.84.1383.
40. Ohgoe, T.; Hirayama, M.; Misawa, T.; Ido, K.; Yamaji, Y.; Imada, M. Ab initio study of superconductivity and inhomogeneity in a Hg-based cuprate superconductor. *Phys. Rev. B* **2020**, *101*, 045124. doi:10.1103/PhysRevB.101.045124.
41. Huang, E.; Mendl, C.B.; Jiang, H.C.; Moritz, B.; Devereaux, T.P. Stripe order from the perspective of the Hubbard model. *npj Quant. Mater.* **2018**, *3*, 22. doi:10.1038/s41535-018-0097-0.
42. Deng, Y.; Kozik, E.; Prokof'ev, N.V.; Svistunov, B.V. Emergent BCS regime of the two-dimensional fermionic Hubbard model: Ground-state phase diagram. *EPL (Europhysics Letters)* **2015**, *110*, 57001. doi:10.1209/0295-5075/110/57001.
43. Šimkovic, F.; Deng, Y.; Kozik, E. Superfluid ground state phase diagram of the two-dimensional Hubbard model in the emergent Bardeen-Cooper-Schrieffer regime. *Phys. Rev. B* **2021**, *104*, L020507. doi:10.1103/PhysRevB.104.L020507.
44. Ponsioen, B.; Chung, S.S.; Corboz, P. Period 4 stripe in the extended two-dimensional Hubbard model. *Phys. Rev. B* **2019**, *100*, 195141. doi:10.1103/PhysRevB.100.195141.
45. Yamase, H.; Eberlein, A.; Metzner, W. Coexistence of Incommensurate Magnetism and Superconductivity in the Two-Dimensional Hubbard Model. *Phys. Rev. Lett.* **2016**, *116*, 096402. doi:10.1103/PhysRevLett.116.096402.
46. Vilardi, D.; Taranto, C.; Metzner, W. Antiferromagnetic and *d*-wave pairing correlations in the strongly interacting two-dimensional Hubbard model from the functional renormalization group. *Phys. Rev. B* **2019**, *99*, 104501. doi:10.1103/PhysRevB.99.104501.
47. Vilardi, D.; Bonetti, P.M.; Metzner, W. Dynamical functional renormalization group computation of order parameters and critical temperatures in the two-dimensional Hubbard model. *Phys. Rev. B* **2020**, *102*, 245128. doi:10.1103/PhysRevB.102.245128.
48. Sordi, G.; Sémon, P.; Haule, K.; Tremblay, A.M.S. Strong Coupling Superconductivity, Pseudogap, and Mott Transition. *Phys. Rev. Lett.* **2012**, *108*, 216401. doi:10.1103/PhysRevLett.108.216401.
49. Sakai, S.; Sangiovanni, G.; Civelli, M.; Motome, Y.; Held, K.; Imada, M. Cluster-size dependence in cellular dynamical mean-field theory. *Phys. Rev. B* **2012**, *85*, 035102. doi:10.1103/PhysRevB.85.035102.
50. Gull, E.; Parcollet, O.; Millis, A.J. Superconductivity and the Pseudogap in the Two-Dimensional Hubbard Model. *Phys. Rev. Lett.* **2013**, *110*, 216405. doi:10.1103/PhysRevLett.110.216405.
51. Gull, E.; Millis, A. Numerical models come of age. *Nature Phys.* **2015**, *11*, 808. doi:10.1038/nphys3501.
52. Harland, M.; Katsnelson, M.I.; Lichtenstein, A.I. Plaquette valence bond theory of high-temperature superconductivity. *Phys. Rev. B* **2016**, *94*, 125133. doi:10.1103/PhysRevB.94.125133.
53. Rømer, A.T.; Maier, T.A.; Kreisel, A.; Eremin, I.; Hirschfeld, P.J.; Andersen, B.M. Pairing in the two-dimensional Hubbard model from weak to strong coupling. *Phys. Rev. Research* **2020**, *2*, 013108. doi:10.1103/PhysRevResearch.2.013108.
54. Otsuki, J.; Hafermann, H.; Lichtenstein, A.I. Superconductivity, antiferromagnetism, and phase separation in the two-dimensional Hubbard model: A dual-fermion approach. *Phys. Rev. B* **2014**, *90*, 235132. doi:10.1103/PhysRevB.90.235132.

55. Kitatani, M.; Schäfer, T.; Aoki, H.; Held, K. Why the critical temperature of high- T_c cuprate superconductors is so low: The importance of the dynamical vertex structure. *Phys. Rev. B* **2019**, *99*, 041115. doi:10.1103/PhysRevB.99.041115.
56. Comin, R.; Damascelli, A. Resonant X-Ray Scattering Studies of Charge Order in Cuprates. *Annual Review of Condensed Matter Physics* **2016**, *7*, 369–405. doi:10.1146/annurev-conmatphys-031115-011401.
57. Wu, T.; Mayaffre, H.; Krämer, S.; Horvatić, M.; Berthier, C.; Hardy, W.N.; Liang, R.; Bonn, D.A.; Julien, M.H. Magnetic-field-induced charge-stripe order in the high-temperature superconductor YBa₂Cu₃O_y. *Nature* **2011**, *477*, 191. doi:10.1038/nature10345.
58. Toschi, A.; Katanin, A.A.; Held, K. Dynamical vertex approximation; A step beyond dynamical mean-field theory. *Phys. Rev. B* **2007**, *75*, 045118. doi:10.1103/PhysRevB.75.045118.
59. Held, K.; Katanin, A.; Toschi, A. Dynamical Vertex Approximation - An Introduction. *Progress of Theoretical Physics (Supplement)* **2008**, *176*, 117.
60. Katanin, A.A.; Toschi, A.; Held, K. Comparing pertinent effects of antiferromagnetic fluctuations in the two- and three-dimensional Hubbard model. *Phys. Rev. B* **2009**, *80*, 075104. doi:10.1103/PhysRevB.80.075104.
61. Rohringer, G.; Hafermann, H.; Toschi, A.; Katanin, A.A.; Antipov, A.E.; Katsnelson, M.I.; Lichtenstein, A.I.; Rubtsov, A.N.; Held, K. Diagrammatic routes to nonlocal correlations beyond dynamical mean field theory. *Rev. Mod. Phys.* **2018**, *90*, 025003. doi:10.1103/RevModPhys.90.025003.
62. Li, D.; Wang, B.Y.; Lee, K.; Harvey, S.P.; Osada, M.; Goodge, B.H.; Kourkoutis, L.F.; Hwang, H.Y. Superconducting Dome in Nd_{1-x}Sr_xNiO₂ Infinite Layer Films, arXiv:2003.08506. *Phys. Rev. Lett.* **2020**, *125*, 027001. doi:10.1103/PhysRevLett.125.027001.
63. Zeng, S.; Tang, C.S.; Yin, X.; Li, C.; Li, M.; Huang, Z.; Hu, J.; Liu, W.; Omar, G.J.; Jani, H.; Lim, Z.S.; Han, K.; Wan, D.; Yang, P.; Pennycook, S.J.; Wee, A.T.S.; Ariando, A. Phase Diagram and Superconducting Dome of Infinite-Layer Nd_{1-x}Sr_xNiO₂ Thin Films. *Phys. Rev. Lett.* **2020**, *125*, 147003. doi:10.1103/PhysRevLett.125.147003.
64. Lee, K.; Wang, B.Y.; Osada, M.; Goodge, B.H.; Wang, T.C.; Lee, Y.; Harvey, S.; Kim, W.J.; Yu, Y.; Murthy, C.; others. Character of the "normal state" of the nickelate superconductors. *arXiv preprint arXiv:2203.02580* **2022**.
65. Lee, K.; Goodge, B.H.; Li, D.; Osada, M.; Wang, B.Y.; Cui, Y.; Kourkoutis, L.F.; Hwang, H.Y. Aspects of the synthesis of thin film superconducting infinite-layer nickelates. *APL Materials* **2020**, *8*, 041107. doi:10.1063/5.0005103.
66. Held, K.; Si, L.; Worm, P.; Janson, O.; Arita, R.; Zhong, Z.; Tomczak, J.M.; Kitatani, M. Phase Diagram of Nickelate Superconductors Calculated by Dynamical Vertex Approximation. *Frontiers in Physics* **2022**, *9*. doi:10.3389/fphy.2021.810394.
67. Malyi, O.I.; Varignon, J.; Zunger, A. Bulk NdNiO₂ is thermodynamically unstable with respect to decomposition while hydrogenation reduces the instability and transforms it from metal to insulator. *Phys. Rev. B* **2022**, *105*, 014106. doi:10.1103/PhysRevB.105.014106.
68. Bernardini, F.; Bosin, A.; Cano, A. Geometric effects in the infinite-layer nickelates. *arXiv preprint arXiv:2110.13580* **2021**.
69. Cui, Y.; Li, C.; Li, Q.; Zhu, X.; Hu, Z.; feng Yang, Y.; Zhang, J.; Yu, R.; Wen, H.H.; Yu, W. NMR Evidence of Antiferromagnetic Spin Fluctuations in Nd_{0.85}Sr_{0.15}NiO₂. *Chin. Phys. Lett.* **2021**, *38*, 067401. doi:10.1088/0256-307x/38/6/067401.
70. Puphal, P.; Pomjakushin, V.; Ortiz, R.A.; Hammoud, S.; Isobe, M.; Keimer, B.; Hepting, M. Investigation of Hydrogen Incorporations in Bulk Infinite-Layer Nickelates. *Frontiers in Physics* **2022**, *10*. doi:10.3389/fphy.2022.842578.
71. Bellaiche, L.; Vanderbilt, D. Virtual crystal approximation revisited: Application to dielectric and piezoelectric properties of perovskites. *Phys. Rev. B* **2000**, *61*, 7877–7882. doi:10.1103/PhysRevB.61.7877.
72. Eckhardt, C.; Hummer, K.; Kresse, G. Indirect-to-direct gap transition in strained and unstrained Sn_xGe_{1-x} alloys. *Phys. Rev. B* **2014**, *89*, 165201. doi:10.1103/PhysRevB.89.165201.
73. Hohenberg, P.; Kohn, W. Inhomogeneous Electron Gas. *Phys. Rev.* **1964**, *136*, B864–B871. doi:10.1103/PhysRev.136.B864.
74. Kohn, W.; Sham, L.J. Self-Consistent Equations Including Exchange and Correlation Effects. *Phys. Rev.* **1965**, *140*, A1133–A1138. doi:10.1103/PhysRev.140.A1133.
75. Kresse, G.; Hafner, J. Ab initio molecular dynamics for liquid metals. *Phys. Rev. B* **1993**, *47*, 558–561. doi:10.1103/PhysRevB.47.558.
76. Kresse, G.; Furthmüller, J. Efficiency of ab-initio total energy calculations for metals and semiconductors using a plane-wave basis set. *Computational materials science* **1996**, *6*, 15–50.
77. Perdew, J.P.; Burke, K.; Ernzerhof, M. Generalized Gradient Approximation Made Simple. *Phys. Rev. Lett.* **1996**, *77*, 3865–3868. doi:10.1103/PhysRevLett.77.3865.
78. Perdew, J.P.; Ruzsinszky, A.; Csonka, G.I.; Vydrov, O.A.; Scuseria, G.E.; Constantin, L.A.; Zhou, X.; Burke, K. Restoring the Density-Gradient Expansion for Exchange in Solids and Surfaces. *Phys. Rev. Lett.* **2008**, *100*, 136406. doi:10.1103/PhysRevLett.100.136406.
79. Anisimov, V.I.; Zaanen, J.; Andersen, O.K. Band theory and Mott insulators: Hubbard U instead of Stoner I. *Phys. Rev. B* **1991**, *44*, 943–954. doi:10.1103/PhysRevB.44.943.
80. Togo, A.; Tanaka, I. First principles phonon calculations in materials science. *Scripta Materialia* **2015**, *108*, 1–5.
81. Baroni, S.; de Gironcoli, S.; Dal Corso, A.; Giannozzi, P. Phonons and related crystal properties from density-functional perturbation theory. *Rev. Mod. Phys.* **2001**, *73*, 515–562. doi:10.1103/RevModPhys.73.515.
82. Blaha, P.; Schwarz, K.; Madsen, G.; Kvasnicka, D.; Luitz, J. wien2k. *An augmented plane wave+ local orbitals program for calculating crystal properties* **2001**.

-
83. Rossi, M.; Osada, M.; Choi, J.; Agrestini, S.; Jost, D.; Lee, Y.; Lu, H.; Wang, B.Y.; Lee, K.; Nag, A.; others. A Broken Translational Symmetry State in an Infinite-Layer Nickelate. *arXiv preprint arXiv:2112.02484* **2021**.
 84. Krieger, G.; Martinelli, L.; Zeng, S.; Chow, L.; Kummer, K.; Arpaia, R.; Sala, M.M.; Brookes, N.; Ariando, A.; Viart, N.; others. Charge and spin order dichotomy in NdNiO₂ driven by SrTiO₃ capping layer. *arXiv preprint arXiv:2112.03341* **2021**.
 85. Ren, X.; Gao, Q.; Zhao, Y.; Luo, H.; Zhou, X.; Zhu, Z. Superconductivity in infinite-layer Pr_{0.8}Sr_{0.2}NiO₂ films on different substrates. *arXiv preprint arXiv:2109.05761* **2021**.
 86. Wang, N.; Yang, M.; Chen, K.; Yang, Z.; Zhang, H.; Zhu, Z.; Uwatoko, Y.; Dong, X.; Jin, K.; Sun, J.; others. Pressure-induced monotonic enhancement of T_c to over 30 K in the superconducting Pr_{0.82}Sr_{0.18}NiO₂ thin films. *arXiv preprint arXiv:2109.12811* **2021**.